

Incoherent signature of internal tides on sea level in idealized numerical simulations

A. L. Ponte and P. Klein,¹

Corresponding author: A. Ponte, LPO, IFREMER / Centre de Brest ZI Pointe du Diable -

CS 10070 29280 Plouzane, FRANCE. (aurelien.ponte@ifremer.fr)

¹Laboratoire de Physique des Océans,

IFREMER-CNRS-IRD-UBO, Plouzané,

France.

This article has been accepted for publication and undergone full peer review but has not been through the copyediting, typesetting, pagination and proofreading process, which may lead to differences between this version and the Version of Record. Please cite this article as doi: 10.1002/2014GL062583

The non persistent phase relationship between internal tides and astronomical forcings, also known as incoherence, has been identified as a major question in the context of future wide-swath satellite altimetry. This study addresses this issue using a novel set of numerical experiments where a plane-wave/low-mode internal tide propagates through a turbulent mesoscale eddy field. These experiments demonstrate the emergence of internal tide incoherence as the eddy turbulence is strengthened. In strongly turbulent situations, the internal tide signature on sea level forms complex interference patterns with large amplifications of the initial internal wave. These patterns evolve more rapidly than the signature of the turbulent eddy field on sea level. The implications of such idealized numerical simulations for wide-swath altimetry are discussed.

1. Motivation

Two satellite altimetric missions which aim at observing sea level with an unprecedented resolution and coverage (10 km, 1 cm accuracy, 75 km wide swath) are currently under development: SWOT led by NASA/CNES [*Fu and Ferrari, 2008*], and, COMPIRA led by JAXA [*Uematsu et al., 2013*]. Both missions are scheduled after 2020. The sea surface height data collected by such missions are expected to capture the mesoscale (50-300 km) and submesoscale (<50 km) turbulent eddy field. Other processes, such as barotropic and baroclinic tides [*Ray and Mitchum, 1997*] and infragravity waves [*Ardhuin et al., 2014*], are known to also have a signature on sea level though and removal of associated signals will be required in order to limit contaminations on estimates of the mesoscale and submesoscale turbulent eddy field from these new altimetric measurements. Removal of barotropic tides from classical nadir-altimetric data is a long-standing problem which has led to significant progress in our ability to map and understand these processes [*Stammer et al., 2014*]. Barotropic tides produce large scale sea level fluctuations of order 1 m that have a close phase relationship with astronomical forcings and are predictable within less than 1 cm in the open ocean [*Stammer et al., 2014; Shriver et al., 2014*]. Baroclinic tides have a smaller signature on sea level, on the order of several cm (i.e. close to that of meso/submesoscale), but do not maintain a fixed phase relationship with astronomical forcings [*Ray and Zaron, 2011; Shriver et al., 2014*]. Departures from this fixed phase relationship is what we call incoherence. Such incoherence affects our ability to predict internal tides and may ultimately compromise our ability to estimate the ocean circulation from high resolution altimetry in regions of low mesoscale-submesoscale activity [*Richman*

et al., 2012]. In these regions, *Richman et al.* [2012] suggest indeed that high frequency phenomena (internal tides in particular) produce significant sea level fluctuations in the 10 to 100 km band (scales newly resolved with SWOT/COMPIRA) that cannot be distinguished from that associated with the mesoscale-submesoscale circulation in altimetric data because of altimeters poor temporal sampling.

Internal tide incoherence has been well observed [*Lerczak et al.*, 2003; *van Haren et al.*, 2004; *Rainville and Pinkel*, 2006a; *Nash et al.*, 2012] and is generally believed to be responsible for the cusp-like shape of detided sea level spectra [*Colosi and Munk*, 2006].

Nash et al. [2012] and *van Haren et al.* [2004] find typical timescales of internal tide incoherence within the 5 to 20 day range.

Internal tide incoherence is attributed to both modulations of stratification close to generation sites [*Kelly and Nash*, 2010; *Zilberman et al.*, 2011] and interactions between internal tides and the background low-frequency circulation during propagation [*Rainville and Pinkel*, 2006a; *Chavanne et al.*, 2010]. Models of varying complexities have been developed in order to reproduce and better understand internal tide incoherence. *Park and Watts* [2006] and *Chavanne et al.* [2010] respectively employed 2D and 3D ray tracing approaches near the Hawaiian area with some success. Regional 3D models [*Zaron and Egbert*, 2014; *Kerry et al.*, 2014] have sufficient resolutions in order to resolve a wide spectrum of internal waves. These models rely on independent reanalysis products or nested approaches in order to incorporate the low-frequency circulation. Some ocean global circulation models resolving simultaneously tides and the low-frequency circulation are emerging and predict an incoherence of the low-mode internal tide [*Arbic et al.*, 2010;

Müller et al., 2012]. The cost and complexity of such realistic models however limits our understanding of mechanisms leading to internal tide incoherence.

The focus here is on understanding interactions between a low-mode internal tide and a low-frequency mesoscale eddy field. Such low-modes carry most of the internal tide energy and are expected to dominate the internal tide signature on sea level [*Ray and Zaron*, 2011]. The semi-diurnal wavelength of the first mode averages globally around 150 km [*Alford and Zhao*, 2007] which is comparable to the scales of energetic mesoscale eddy structures. In a shallow-water framework, *Ward and Dewar* [2010] investigated the scattering, in horizontal wavenumber space, of a unidirectional plane wave by a geostrophically balanced turbulent flow and showed how the pace of the scattering increased with the strength of the balanced turbulence and the wave frequency. When vertical variability is introduced, *Dunphy and Lamb* [2014] described with 3D numerical simulations how interactions between low-mode internal tides and isolated barotropic and baroclinic eddies not only horizontally deflect internal tides but can also scatter them in vertical mode space.

Another level of complexity is here added by considering the propagation of a mode one internal tide across a fully turbulent mesoscale/submesoscale field, i.e. involving a large number of strongly interacting eddies. The goal is to illustrate how the internal tide becomes progressively incoherent across the jet and how this incoherence varies with the strength of the mesoscale turbulence. The experimental setup is described in section 2.

The focus is on the signature of internal tides on sea level and the corresponding analysis

is described in section 3. Results are then presented (section 4). Section 5 concludes and discusses future perspectives.

2. Numerical setting

The numerical setting is that of a baroclinic unstable jet in a zonal β -plane channel centered around 45°N . The numerical model is the Regional Oceanic Modeling System (ROMS, see *Shchepkin and McWilliams* [2005]) which solves the hydrostatic primitive equations. The domain is $1024 \text{ km} \times 3072 \text{ km}$ and its depth is 4 km. The horizontal resolution is 4 km and there are 50 vertical levels with a vertical resolution of 7 m close to the surface and 350 m at depth. The model is closed at the northern and southern boundaries and periodic in the zonal direction. Density is linearly related to temperature with salinity being held constant and uniform. Vertical mixing is based on a K-profile parametrization (KPP, see footnote of *Klein et al.* [2008]). Horizontal mixing uses a Laplacian operator with a coefficient of $3.5 \text{ m}^2 \text{ s}^{-1}$.

Simulations are initialised with a perturbed eastward zonal jet. The jet is unstable by a baroclinic instability of the Phillips type associated with the reversal of the meridional potential vorticity gradient at 1000 depth as in *Ponte and Klein* [2013]. The resulting eddy turbulence (Fig. 1a) is later maintained by relaxing the zonal mean current toward the unperturbed initial jet on a 100 day timescale. Such configuration leads to a steep k^{-5} spectrum of sea level (with k the wavenumber), as predicted by classical theories of quasigeostrophic turbulence [*Charney*, 1971]. Simulations with varying levels of turbulent mesoscale intensity are conducted as shown by meridional sections of time-averaged kinetic energy of the detided surface flow (Fig 2, see section 3 for a description of the

detiding procedure). Variations of the mesoscale intensity are achieved by modulating the initial south/north difference of density profiles. Four simulations with increasing level of mesoscale activity are thereby produced and labelled KE1 to KE4 (Fig 2). The meridional extent of the mesoscale turbulence is controlled by damping zonal anomalies of currents with a 10 days relaxation timescale within 600 km wide areas at the southern and northern end of the domain (not shown on Fig. 1). This damping inhibits interferences between the mesoscale turbulence and the internal tide wavemaker (described below) while not affecting the initial propagation of the zonally-uniform internal wave.

The original aspect of these simulations comes from the addition of an idealized source of internal tide located southward to the jet (Fig. 1). The internal tide is generated by a zonally uniform, time periodic, meridional force \mathcal{F}_v :

$$\mathcal{F}_v = f_0 \sin(\omega t) e^{-(y-y_{\text{wm}})^2/\Delta_{\text{wm}}^2} \phi_1(z), \quad (1)$$

where $f_0 = 1.2 \cdot 10^{-5} \text{ m s}^{-2}$ is the amplitude of the forcing and ϕ_1 is the velocity/pressure modal structure of first baroclinic vertical mode computed with the south profile of stratification [Gill and Clarke, 1974]. The forcing frequency ω is 2 days^{-1} , i.e. typical of a semidiurnal tide. The forcing is centered around $y_{\text{wm}} = 400 \text{ km}$ and its meridional width Δ_{wm} is 10 km (Fig. 1). The forcing is initially ramped up to its full value over a time scale of about 5 days. The internal wave thereby produced is a plane-wave with a wavelength of about 150 km consistent with the baroclinic mode one dispersion relation, and, a 2 cm signature on sea level (Fig. 1b). The energy flux associated with the internal tide is ap-

proximately 10 kW m^{-1} which is typical of fluxes nearby strong internal tides generation sites [Rainville and Pinkel, 2006b].

3. Analysis

One goal of the present work is to understand interactions between internal tides and a fully turbulent eddy field. To do so, we focus on model output collected along a meridional section at the center of the channel ($x = 512 \text{ km}$). Sea level and surface variables such as current and relative vorticity are stored every half hour.

The resulting dataset is analysed over one-day windows in order to distinguish mesoscale and tidal contributions. This is achieved with least-square fits over each one-day window of the following form:

$$\eta = \underbrace{\eta_m + \eta'_m t}_{\text{mesoscale}} + \underbrace{\eta_{\cos} \cos \omega t + \eta_{\sin} \sin \omega t}_{\text{tide}}, \quad (2)$$

where η_m and $\eta'_m t$ capture the slow mesoscale turbulence, i.e detided data and $\eta_{\cos} \cos \omega t$ and $\eta_{\sin} \sin \omega t$ represent the fast tidal flow. Windows are one day apart and the remainder of the present work consists of an analysis of the fit coefficient time series (with emphasis on η_m, η_{\cos}). Such a fit captures on average 95% of the sea level variance. The uncaptured part of the variance due to the presence of higher tidal harmonics or high frequency motions generated by the mesoscale turbulence is therefore small. Note that the linear trend $\eta'_m t$ is small over one day compared to the mean part η_m but its inclusion limits projections of mesoscale variations onto η_{\sin} .

Mesoscale sea level fluctuations η_m are largest at the center of the jet for both KE2 and KE4 (Fig. 3, top). KE4 well exhibits weaker fluctuations south and north of the jet

associated with Rossby waves. In both cases, the evolution before day 20 of the sea level tidal harmonic η_{\cos} reflects the internal tide initial northward propagation (Fig. 3). Its sinusoidal shape as a function of y is characteristic of the internal tide plane wave nature. This η_{\cos} plane wave pattern remains steady in time up until the zonal jet destabilises (through baroclinic instability) around day 50 (200) for KE4 (KE2) and becomes turbulent. The time evolution of the harmonic sea level η_{\cos} becomes erratic from then on with most intense fluctuations occurring at the center and north of the turbulent jet. Large amplifications of the internal tide occurs for KE4 with maximum sea level oscillations for η_{\cos} up to 10 cm, i.e. 5 times the initial internal tide signature on sea level. In a simpler setting, *Dunphy and Lamb* [2014] already observed similar focusing effects. Milder perturbations of the harmonic also occur south of the jet indicating that part of the internal tide is reflected back by the mesoscale eddy field. Variations of harmonic sea level are weaker for KE2 even though values up to 4 cm are reached, i.e. twice initial values. Finally, time variations of the tidal harmonic are visually slower for KE2 than for KE4, which is further quantified in section 4.

4. Results

Time mean and standard deviations of the sea level tidal harmonic η_{\cos} have been computed along the meridional section ($x = 512$ km) in order to quantify the incoherence of the internal tide signature on sea level (Fig 4). For weak mesoscale turbulence (KE1), the internal tide propagates northward unaffected as indicated by the quasi-sinusoidal shape of mean harmonics. Variations around mean values as measured by the rms do not exceed 20% of the amplitude of tidal sea level fluctuations. The internal tide is thus

coherent, i.e. its phase with respect to internal wave forcing is fixed, and expected to be largely predictable in such a case. For moderate levels of turbulence (KE2), incoherence emerges as tidal harmonics rms are now comparable to their mean values. Mean values reflect nonetheless a well-defined northward propagation of the signal and we conclude the tidal sea level is partially coherent with the forcing. For larger turbulence levels (KE3 and KE4), mean values of the harmonic have decreased to the point that they are statistically undistinguishable from zero north of the jet. The rms of harmonic sea level are comparable to the input internal wave amplitude (2 cm), which reflect the fully incoherent nature of tidal sea level fluctuations there. Incoherence has also emerged southward of the jet as indicated by the larger rms and as already observed on Fig 3. Following *Shriver et al.* [2014], normalized rms of complex sea level amplitudes ($\eta_{\cos} + i\eta_{\sin}$) are averaged north of the turbulent jet with a 1 mm threshold on the mean amplitude. These values (0.1, 0.8, 9.7, and, 11.0 for KE1 to KE4 respectively) encompass those found by *Shriver et al.* [2014].

Fig. 3 suggests that variations of sea level tidal harmonics at a given y location are more rapid for KE4 than for KE2. A quantification for this observation is provided by the decorrelation timescale $\tau_{\eta,\cos}$ of the tidal harmonic η_{\cos} defined as the 0.5 crossing of its time autocorrelation function. The harmonic's decorrelation timescale is averaged spatially from the center of the jet up to the starting location of the northern sponge layer. This timescale is compared with the decorrelation timescale of the detided sea level $\tau_{\eta,m}$ and that of detided surface relative vorticity $\tau_{\xi,m}$. These timescales are averaged over the region where the turbulent eddy kinetic energy is within 90% of its peak value, i.e. in the

central part of the turbulent jet. For a weakly turbulent jet (KE1), the tidal harmonic η_{\cos} evolves on a slow 60 days timescale approximately (Fig. 5). For moderately turbulent eddy fields (KE2), the tidal harmonic decorrelation timescale decreases down to 15 days. For strongly turbulent eddy fields (KE3 and KE4), the sea level tidal harmonic evolves on extremely short timescales (6 days for KE3 and 2.5 days for KE4). These timescales cover the range of values experimentally observed by *Nash et al.* [2012] and *van Haren et al.* [2004] even though the comparison could be considered as bold at this point considering the difference of perspective. In all four cases, the decorrelation timescale of the tidal harmonic is lower than that of the detided sea level and longer than that of detided relative vorticity (Fig. 5). For weakly turbulent jet, the decorrelation timescale is close to that of sea level. For strongly turbulent jets it becomes much smaller, by up to a factor 5 and comparable to that of relative vorticity for KE4. Tidal harmonics and mesoscale decorrelation timescales are overall similar which supports an interpretation in terms of scattering by a slowly evolving eddy field and is a relevant result for high resolution altimetry.

5. Discussion and perspectives

Present results illustrate the emergence of internal tide incoherence as the strength of the mesoscale turbulence encountered by an idealized low-mode internal tide is increased. For strongly turbulent situations, the internal tide signature on sea level is fully incoherent, that is tidal harmonics η_{\cos} are highly variable in time with mean values statistically undistinguishable from zero. These results are expected to be sensitive to the choice of internal wave vertical mode number. Higher modes are indeed slower and more likely to

be affected by mesoscale turbulence compared to low modes and preliminary numerical investigations concur. On the other hand the signature of higher modes on sea level is weaker which makes them less relevant to satellite altimetry than low modes [*Ray and Zaron, 2011*]. The vertical structure of the mesoscale turbulence may also affect present results [*Dunphy and Lamb, 2014*].

A quantitative explanation for present results awaits further studies. Internal tide incoherence is the result of multiple interactions between the internal tide and complex-shaped time-evolving mesoscale structures. This work suggests that a fundamental ingredient leading to incoherence is the strength of mesoscale structures which has been shown to control the magnitude of internal wave deflections [*Ward and Dewar, 2010; Dunphy and Lamb, 2014*]. Another essential ingredient is the time dependence of the mesoscale turbulence. Steady mesoscale structures would indeed lead to a potentially complicated yet coherent interference pattern of internal tide. In present numerical simulations, the strength and time dependence of the mesoscale turbulence however covary (Fig. 5), which makes it difficult to identify their contributions to incoherences reported here.

A predictive model for the propagation of low-mode internal tides within a turbulent eddy field would constitute a lighter tool in order to make progress on these fundamental issues. Such a model is the subject of ongoing research [*Kelly, 2014*] and would be most valuable to address several questions relevant to high resolution wide-swath altimetry: to what extent can we predict the propagation of a low-mode internal tides through a mesoscale eddy field, can we provide a remedy for internal tide incoherence and at what

cost? Idealized simulations such as that presented here will constitute critical tools in order to answer these questions.

Acknowledgments. We acknowledge the support of IFREMER, CNRS, the Agence Nationale pour la Recherche [ANR-10-LABX-19-01 (LabexMER)], the CNES's SWOT mission, and, the PRACE Research Infrastructure through allocation 2014102346.

References

Alford, M. H., and Z. Zhao (2007), Global Patterns of Low-Mode Internal-Wave Propagation. Part II: Group Velocity., *J. Phys. Oceanogr.*, *37*, 1849–1858.

Arbic, B. K., A. J. Wallcraft, and E. J. Metzger (2010), Concurrent simulation of the eddying general circulation and tides in a global ocean model, *Ocean Modelling*, *32*, 175–187.

Ardhuin, F., A. Rawat, and J. Aucan (2014), A numerical model for free infragravity waves: Definition and validation at regional and global scales, *Ocean Modelling*, *77*, 20–32.

Charney, J. G. (1971), Geostrophic Turbulence, *J. Atmos. Sci.*, *28*, 1087–1095.

Chavanne, C., P. Flament, D. Luther, and K.-W. Gurgel (2010), The surface expression of semi-diurnal internal tides near a strong source at hawaii. part ii: Interactions with mesoscale currents., *J. Phys. Oceanogr.*, *40*, 1180–1200.

Colosi, J. A., and W. Munk (2006), Tales of the Venerable Honolulu Tide Gauge, *J. Phys. Oceanogr.*, *36*, 967–996.

Dunphy, M., and K. G. Lamb (2014), Focusing and vertical mode scattering of the first mode internal tide by mesoscale eddy interaction, *J. Geophys. Res.*, *119*, 523–536.

Fu, L. L., and R. Ferrari (2008), Observing oceanic submesoscale processes from space, *Eos*, *89*(48), 488.

Gill, A. E., and A. J. Clarke (1974), Wind-induced upwelling, coastal currents and sea-level changes, *Deep-Sea Research*, *21*, 325–345.

Kelly, S. M. (2014), Low-mode internal tides in background flows, in *Nonlinear Effects in Internal Waves Conference*.

Kelly, S. M., and J. D. Nash (2010), Internal-tide generation and destruction by shoaling internal tides, *Geophysical Research Letters*, *37*(L23611).

Kerry, C. G., B. S. Powell, and G. S. Carter (2014), The Impact of Subtidal Circulation on Internal Tide Generation and Propagation in the Philippine sea, *J. Phys. Oceanogr.*, *44*, 1386–1405.

Klein, P., B. L. Hua, G. Lapeyre, X. Capet, S. L. Gentil, and H. Sasaki (2008), Upper ocean turbulence from high-resolution 3d simulations, *J. Phys. Oceanogr.*, *38*, 1748–1762.

Lerczak, J. A., C. D. Winant, and M. C. Hendershott (2003), Observations of the semidiurnal internal tide on the southern California slope and shelf, *J. Geophys. Res.*, *108*(C3).

Müller, M., J. Y. Cherniawsky, M. G. G. Foreman, and J. von Storch (2012), Global m_2 internal tide and its seasonal variability from high resolution circulation and tide modeling, *Geophysical Research Letters*, *39*(L19607).

Nash, J. D., S. M. Kelly, E. L. Shroyer, J. N. Moum, and T. F. Duda (2012), The Unpredictable Nature of Internal Tides on Continental Shelves, *J. Phys. Oceanogr.*, *42*, 1981–2000.

Park, J.-H., and D. R. Watts (2006), Internal Tides in the Southwestern Japan/East Sea, *J. Phys. Oceanogr.*, *36*, 22–34.

Ponte, A. L., and P. Klein (2013), Reconstruction of the upper ocean 3d dynamics from high resolution sea surface height, *Ocean Dynamics*, *63*(7), 777–791.

Rainville, L., and R. Pinkel (2006a), Propagation of Low-Mode Internal Waves through the Ocean, *J. Phys. Oceanogr.*, *36*, 1220–1236.

Rainville, L., and R. Pinkel (2006b), Baroclinic Energy Flux at the Hawaiian Ridge: Observations from the R/P FLIP, *J. Phys. Oceanogr.*, *36*, 1104–1122.

Ray, R., and G. Mitchum (1997), Surface manifestation of internal tides in the deep ocean: observations from altimetry and island gauges, *Progress in Oceanography*, *40*(1-4), 135–162.

Ray, R. D., and E. D. Zaron (2011), Non-stationary internal tides observed with satellite altimetry, *Geophysical Research Letters*, *38*.

Richman, J. G., B. K. Arbic, J. F. Shriver, and E. J. Metzger (2012), Inferring dynamics from the wavenumber spectra of an eddying global ocean model with embedded tides, *J. Geophys. Res.*, *117*(C12012).

Shchepetkin, A. F., and J. C. McWilliams (2005), The regional ocean modeling system: A split-explicit, free-surface, topography-following coordinates ocean model, *Ocean Modelling*, *9*, 347–404.

- Shriver, J. F., J. G. Richman, and B. K. Arbic (2014), How stationary are the internal tides in a high resolution global ocean circulation model?, *J. Geophys. Res.*, *119*(5), 2769–2787.
- Stammer, D., R. D. Ray, O. B. Andersen, B. K. Arbic, W. Bosch, L. Carrère, Y. Cheng, D. S. Chinn, B. D. Dushaw, G. D. Egbert, S. Y. Erofeeva, H. S. Fok, J. A. M. Green, S. Griffiths, M. A. King, V. Lapin, F. G. Lemoine, S. B. Luthcke, F. Lyard, J. Morison, M. Müller, L. Padman, J. G. Richman, J. F. Shriver, C. K. Shum, E. Taguchi, and Y. Yi (2014), Accuracy assessment of global barotropic ocean tide models, *Reviews of Geophysics*, doi:10.1002/2014RG000450.
- Uematsu, A., R. Nakamura, Y. Nakajima, Y. Rajima, and J. C. Team (2013), X-band interferometric sar sensor for the japanese altimetry mission, in *Geoscience and Remote Sensing Symposium (IGARSS)*, pp. 2943–2946.
- van Haren, H., L. S. Laurent, and D. Marshall (2004), Small and mesoscale processes and their impact on the large scale: an introduction, *Deep-Sea Research II*, *51*, 2883–2887.
- Ward M. L. and W. K. Dewar (2010), Scattering of gravity waves by potential vorticity in a shallow-water fluid, *J. Fluid Mech.*, *663*, 478–506.
- Young, W. R., and M. Ben Jelloul (1997), Propagation of near-inertial oscillations through a geostrophic flow, *Journal of Marine Research*, *55*, 735–766.
- Zaron, E. D., and G. D. Egbert (2014), Time-Variable Refraction of the Internal Tide at the Hawaiian Ridge, *J. Phys. Oceanogr.*, *44*, 538–557.
- Zilberman, N. V., M. A. Merrifield, G. S. Carter, D. S. Luther, M. D. Levine, and T. J. Boyd (2011), Incoherent Nature of M_2 Tides at the Hawaiian Ridge, *J. Phys. Oceanogr.*, *41*, 2021–2036.

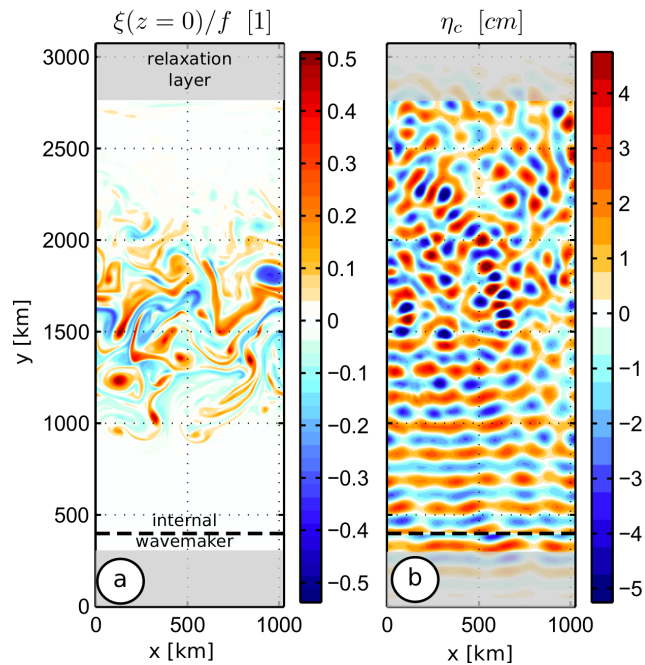


Figure 1. Overview of the numerical simulation KE4 (most intense mesoscale turbulence) at $t = 500$ day. a/ Detided surface relative vorticity $\xi(z = 0)$, normalized by the Coriolis frequency. b/ Tidal harmonic of sea level η_{\cos} . The location of the internal tide wavemaker is represented by the horizontal dashed line. Grey shadings represent areas where all fields are strongly relaxed toward initial values.

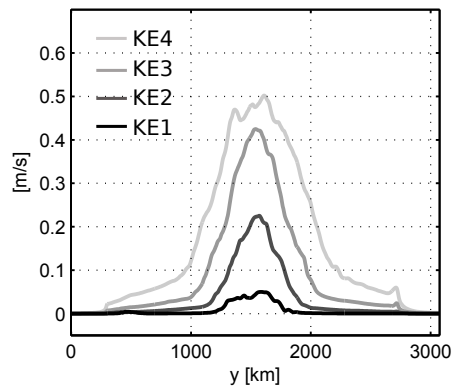


Figure 2. Meridional section of the square root of the time-averaged detided kinetic energy at $z = 0$ and $x = 512$ km. Grey shadings represent simulations with increasing levels of mesoscale turbulence intensity, from black (KE1) to light grey (KE4).

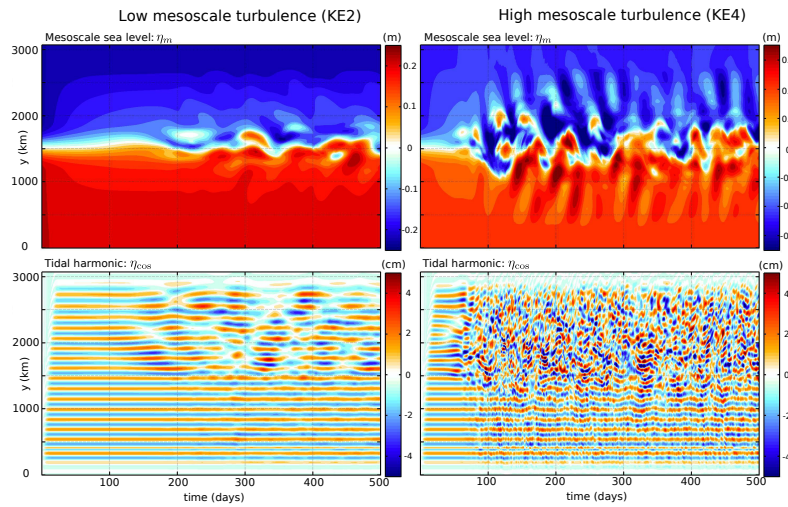


Figure 3. Mesoscale (η_m , upper row) and harmonic tidal (η_{\cos} , lower row) contributions to sea level as a function of time and space (y) for KE2 (left) and KE4 (right) at $x = 512$ km. The colorbar for η_{\cos} and KE4 is saturated, as amplitudes actually reach values up to 10 cm.

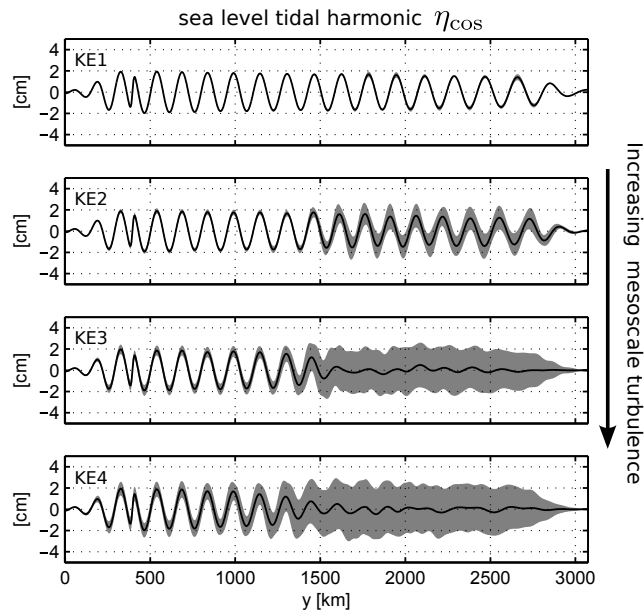


Figure 4. Time-averaged value of the harmonic sea level η_{cos} at $x = 512$ km and as a function of y for simulations KE1 to KE4. Grey shadings represent values 1.3 times the standard deviation away from mean values (80% percentile of a Gaussian variable).

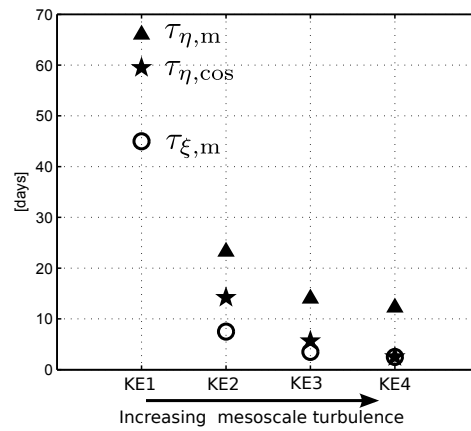


Figure 5. Decorrelation timescales (defined as the 0.5 crossings of autocorrelation functions) of the sea level tidal harmonic ($\tau_{\eta, \text{cos}}$, pentagrams), of the mesoscale sea level ($\tau_{\eta, \text{m}}$, triangles), and, of the mesoscale relative vorticity ($\tau_{\xi, \text{m}}$, circles).